Article

Improving Thermosensitive Bioink Scaffold Fabrication with a Temperature-Regulated Printhead in Robot-Assisted *In Situ* Bioprinting System

Zitong Wang, Li Lin, Xiangyu Li, Quan Zhang, Xuelian Mi, Bide Xu, Yuanjing Xu, Tongyou Liu, Yuling Shen, Zan Wang, Neng Xie, and Jinwu Wang*

Read Online

ACCESS | Metrics & More | Article Recommendations | Supporting Information

ABSTRACT: *In situ* bioprinting enables precise 3D printing inside the human body using modified bioprinters with thermosensitive bioinks such as gelatin methacrylate (GelMA). However, these devices lack refined temperature-regulated mechanisms essential for ensuring bioink viscosity, as compared to traditional bio-3D printers. Addressing this challenge, this study presents a temperature-regulated printhead designed to improve the fabrication of thermosensitive bioink scaffolds in *in situ* bioprinting, integrated into a UR5 robotic arm. Featuring a closed-loop system, it achieves a temperature steady error of 1 °C and a response time of approximately 1 min. The effectiveness of the printer was validated by bioprinting multilayer lattice 3D bioscaffolds. Comparisons were made with or without temperature control using different concentrations of GelMA + LAP. The deformation of the bioscaffolds under both conditions was analyzed, and cell culture tests were conducted to verify viability. Additionally, the rheology and mechanical properties of GelMA were tested. A final preliminary *in situ* bioprinting experiment was conducted on a model of a damaged femur to demonstrate practical application. The fabrication of this printhead is entirely open source, facilitating easy modifications to accommodate various robotic arms. We encourage readers to advance this prototype for application in increasingly complex *in situ* bioprinting situations, especially those utilizing thermosensitive bioinks.
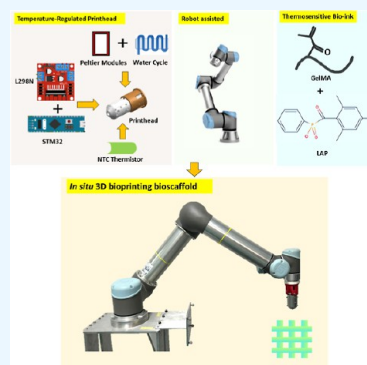
1. INTRODUCTION

Biological 3D printing is revolutionizing regenerative medicine and personalized healthcare by fabricating living tissues that mimic human body parts.[1−5] This innovation enables the production of tailor-made implants and systems, significantly advancing treatments in tissue regeneration, with notable applications in skin, cardiac, and neural engineering.[6−10] At the core of biological 3D printing is the use of hydrogel-based bioinks, with GelMA and Pluronic F-127 emerging as promising thermosensitive materials due to their biocompatibility, adjustable physicochemical properties, and efficient photo-cross-linkability.[11] GelMA, a widely used hydrogel, exhibits increased viscosity and gel-like behavior at lower temperatures, facilitating extrusion and printing; however, at higher temperatures, its viscosity decreases, making it too fluid and unsuitable for printing. Therefore, it is optimal to maintain GelMA at temperatures below room temperature.[12] Pluronic F-127, a thermoresponsive polymer, remains in a highly liquid state at lower temperatures (below 10 °C), making it unsuitable for printing as it extrudes as a liquid. For effective printing, Pluronic F-127 should be maintained at temperatures just below its gelation point but not too low to avoid excessive fluidity.[13] Both materials require precise thermal control for optimal print quality and structural integrity.

Advancing from traditional ectopic bioprinters, the development of *in situ* biological 3D printing has emerged as a transformative approach in the field, enabling direct tissue fabrication within the patient's body, which improves cell health and surgery results and minimizes the rejection risks associated with traditional *ex vivo* bioprinters.[14−18] This area is rapidly evolving, with research concentrated on developing hand-held and robotic bioprinters for highly customized therapeutic approaches.[19−21] Recent progress in *in situ* bioprinting has led to the creation of intuitive hand-held bioprinting devices, such as biopens and bioguns.[22,23] These innovations simplify the bioprinting process, significantly reducing the requirement for comprehensive training. Concurrently, the introduction of robotic-assisted bioprinting seeks to address instability associated with hand-held bioprinters.[24−26] By utilizing robotic arms, this approach enhances the accuracy of the bioprinting process, ensuring more precise
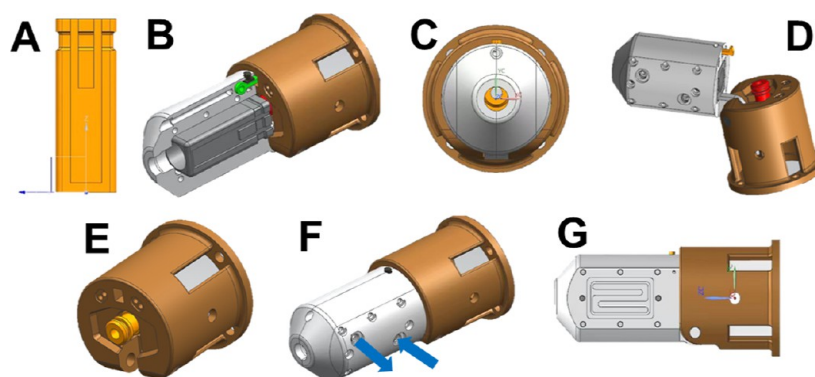
Figure 1. 3D design schematic of the temperature-regulated printhead. (A) The aluminum alloy cartridge holds a 5 mL bioink syringe, with grooves for two 29 × 9.8 mm Peltier modules. (B) 3D assembly view of the printhead, all components are integrated with screws. (C) Top view (D) the hinge allows for easy bioink replication by opening the printhead, while a buckle serves as a switch to secure it. (E) The end bracket features a central piston for pneumatic supply connection. (F) Complete printhead assembly. (G) The cross-section shows an S-shaped cooling cycle for heat dissipation from Peltier modules.

deposition of biological materials.[27−30] However, the development of efficient temperature regulation systems for *in situ* bioprinting has seen limited research. Despite the focus on creating functional *ex vivo* 3D bioprinters with bioink temperature control, significant limitations exist for their *in situ* applications: (1) the devices are too large, rendering them unsuitable for transplantation into target environments;[31] (2) they depend on external sensors and control systems for temperature regulation, which are not adaptable to environments that cannot be directly monitored;[32] (3) there is no assurance that these devices will not adversely affect the surrounding biological tissues.[33] Fortunato *et al.* (2023) highlighted challenges in extending the duration of experiments using an automated photo-cross-linking system in robotic *in situ* bioprinting due to the absence of a temperature-regulated mechanism.[34] Despite initial cooling, GelMA bioinks would eventually liquefy when exposed to room temperatures, limiting experiment times to under 30 min. Alternatively, Garciamendez-Mijares *et al.* (2023) led to the creation of an economical temperature-controlled printhead, designed for integration with the modified Anet A8 3D printer.[35] Furthermore, Sanz-Garcia *et al.* (2020) successfully adapted their do-it-yourself (DIY) temperature-controlled printhead for compatibility with three distinct brands of 3D printers.[36] Nevertheless, these two temperature control systems are designed specifically for standard *ex vivo* 3D bioprinters (an enclosed printing chamber to print tissue and transplant it into the wounded area) and fail to meet the needs of *in situ* bioprinters, indicating a gap in current bioprinting technology.

Addressing this gap, this study introduces a cost-effective temperature-regulated printhead designed for optimizing bioscaffold structure in *in situ* robot-assisted bioprinting applications ($600). Compared to existing temperature-controlled printheads, the structure of the temperature-controlled printhead in this study is specifically designed for mounting on a robotic arm. Table S1 in the Supporting Information lists the printhead names, functions, application scenarios, bioink temperature regulation capabilities, and compatibility with robotic arms. Currently, temperature-controlled printheads are only installed on conventional *ex vivo* box-type bioprinters. As shown in Table S1, there are no temperature-controlled printheads for robotic arm-assisted *in situ* bioprinting, and our research aims to fill this gap.

We open-source the design principles, fabrication processes, control strategies, and biological assessments of our prototype, aiming to enable widespread customization of the printhead. The interior of the printhead contains Peltier modules that can regulate the environmental temperature of the syringe filled with bioink between 0 and 40 °C range, thereby maintaining its ideal viscosity for high-resolution printing. Steady-state thermal analysis and response tests validated the printhead's temperature control ability and efficiency. Mounted a UR5 arm, the printhead printed GelMA scaffolds, then underwent cell viability testing. Additionally, a preliminary experiment on a 3D-printed femur model assessed the clinical potential of the temperature-regulated printing system.

2. METHODS AND MATERIALS

2.1. Printhead Structure Design and Mount Fabrication. In this study, an advanced printhead was designed with a temperature regulation mechanism to address the issue of maintaining a constant bioink's temperature in *in situ* 3D bioprinting. This printhead is engineered to maintain the temperature of biological materials within a 5 mL plastic syringe, offering affordability, compactness, and ease of disassembly. The design was drafted using Unigraphics NX 12.0., and underwent precision machining from aluminum alloy (6061, T6) for its excellent thermal conductivity. For fabrication, the printhead integrates a cartridge, dual Peltier modules (29 × 9.8 mm), two S-shaped cooling shells, and casings with straight fittings, as depicted in Figure 1. The aluminum alloy cartridge enhances thermal conductivity by wrapping the bioink syringe, while Peltier modules embedded in the cartridge with thermal grease enable precise temperature control through heating and cooling (Figure 1A−C). A water-cooling shell connected to a custom pump system at the Peltier modules' rear efficiently dissipates heat (Figure 1G). Straight fittings on the outside shell are used for water connections. The lower port is the water inlet, and the upper port is the water outlet (Figure 1F). Accessories for ease of use and maintenance, such as a fixed bracket, a buckle, and a quick-access articulated hinge for bioink replacement, are 3D printed with PLA+ material (Figure 1D,E). Thermal efficiency was validated through ANSYS Workbench simulations. 2D engineering drawings and assembly models are available in Supporting Information (see 2D engineering drawings.doc and assembly.stp).
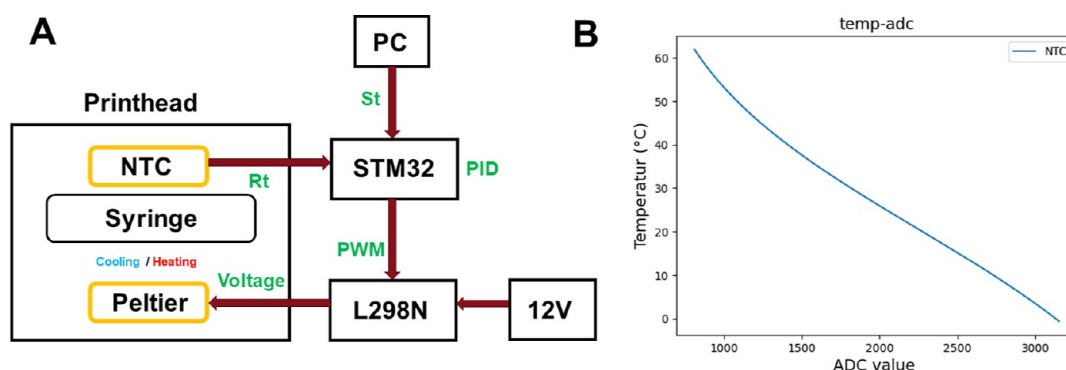
Figure 2. (A) The temperature-regulated system. A 100 K NTC thermistor collects the bioink syringe's Rt inside the printhead, relays it to an STM32 that performs a PID algorithm with St from a PC. The STM32's PWM output controls a L298N to modulate a 12 V power supply for the Peltier modules, enabling precise heating and cooling. (B) The relationship between the temperature measured by an NTC thermistor and the corresponding ADC values.

2.2. Design of Temperature Control System.

In alignment with the design principles specified in Section 2.1, the printhead integrates Peltier modules for refined thermal management. Half of the temperature control system is externalized to maintain the compactness and efficiency of the printhead, as shown in Figure 2A. Despite the recent popularity of machine learning (ML) for enhancing additive manufacturing quality control,[37,38] a closed-loop control system (PID control) was chosen for the thermally controlled print head in this study. This decision was based on the following considerations: PID control offers high reliability and real-time performance, ensuring stable print head temperature, which is crucial for bioink performance. The PID algorithm is mature, simple to implement, widely used in industrial control, and easy to integrate into resource-constrained systems like STM32. In contrast, ML algorithms, while flexible, require high computational power and storage, making them unsuitable for embedded systems. At the heart of this setup is the STM32F103C8T6Microcontroller Unit (MCU). The system is divided into two main parts: real-time temperature data (Rt) collection with a 100 K NTC (negative temperature coefficient) thermistor (Xindongxin Weiye Electronics, Guangzhou, China) placed outside the syringe and implementing the PID (Proportional-Integral-Derivative) temperature control algorithm. The MCU connects to PC software *via* a TTL serial port, allowing Rt and setting temperature (St) modifications to user preferences. The comprehensive temperature value list of NTC thermistor (ranging from −40 to 250 °C) and corresponding resistance values are provided by the manufacturer. The relationship between temperature and resistance values has been modeled

$$R = 311.99 \times e^{-0.05t} + 10.99 \tag{1}$$

where R is the resistance value and t is the temperature value. Upon recognizing temperature fluctuations, the NTC thermistor's resistance will change, which generates a voltage indicative of the surrounding temperature. The STM32's ADC (analog-to-digital converter) channel captures this signal, using its 12 bit resolution to convert analog voltage into digital value ranging from 0 to 4095. The mathematical relationship between the R and the corresponding ADC digital output is

$$ADC = \frac{4096 \times R}{R + R_i} \tag{2}$$

where 4096 is the maximum resolution of the ADC and R_i is the 100 K series shunt, other shunts can also be selected. To replace R in both (1) and (2), we can calculate the relational equation between ADC value and temperature value

$$t = -19.8413 \ln\left(\frac{0.3205 \times ADC + 0.0352}{ADC - 4096}\right) \tag{3}$$

Figure 2B shows the curve from eq 3, implemented in STM32 programming to obtain temperature readings. Choosing an ultrathin NTC thermistor enhances printhead versatility and allows for seamless integration across various design configurations.

The PID algorithm, essential for feedback control, is utilized extensively in various engineering fields to stabilize and regulate systems.[39] In this study, the PID control parameters—proportional (K_p), integral (K_i), and differential (K_d) gains—were finely adjusted to manage thermal regulation accurately. The algorithm, developed in Keil5MDK and deployed on the STM32 microcontroller, interprets temperature readings from an NTC thermistor and modulates a PWM signal. This signal controls an L298N H-bridge driver, which in turn adjusts the temperature of the Peltier modules, ensuring alignment with predetermined targets (St) by comparing them to Rt. The integrated code including harnessing the NTC thermistor for temperature data acquisition and PID algorithm is thoroughly documented in the Supporting Information (see stm32 PID & NTC.zip).

2.3. Temperature Control Performance.

The thermal performance was investigated of the printhead by analyzing its temperature stability and the efficiency of its heating and cooling cycles. The NTC thermistor's data collection with an STM32 was first calibrated with a TP101 temperature probe (Shenzhen Shenghui Tech.). Both sensors, placed in four water cups, recorded temperatures for a minute. After verifying the NTC thermistor's temperature sensing accuracy, the Peltier modules under PID algorithm control were manipulated to modify the starting room temperature of 18.8 °C to targeted values (cooling to 5 and 10 °C and heating to 25 and 30 °C). The NTC thermistor tracked the Rt changes at the location of the bioink syringe. Another test recorded the printhead's temperature changes in five-degree increments, offering a detailed examination of its thermal response and efficiency during both the heating and cooling phases, thereby providing more insights into its operational performance.

2.4. Inks Preparation, Rheological Characterization, and Mechanical Properties Tests.

GelMA was selected as bioink in the following printing experiments due to its temperature-responsive rheological properties at different temperatures. Several studies have analyzed GelMA hydrogels' performance across key temperature ranges.[40−42] Different ratio GelMA solution was prepared in-house, following protocols from similar bioprinting research.[43] The Gelatin was dissolved in Dulbecco's phosphate-buffered saline (DPBS, Sigma-Aldrich, USA) at 60 °C for 1 h. This GelMA was combined with lithium phenyl2,4,6-trimethylbenzoylphosphinate (LAP) (Cellink, Sweden) photoinitiator. The final ink was stored at 4 °C in a refrigerator until used for bioprinting. Before being fitted into the printhead, the GelMA is heated in a water bath at 37 °C for 1 h.

To better understand the effect of temperature on the bioink's rheology, which is directly related to the results for bioprinted scaffolds. The rheology properties were measured on a Discovery HR 20 rotational rheometer (TA Instruments, New Castle, DE, USA). Ten mL solutions of GelMA + LAP, each at 5 different concentrations, were subjected to a controlled cooling process from 40 to 10 °C at a rate of 1 °C per minute and a constant shear rate of 1 s^{-1}. During this cooling ramp, the viscosity (η), storage modulus (G'), and loss modulus (G'') were continuously recorded to generate respective temperature-dependent profiles. The hydrogel samples for mechanical properties tests were extruded into cylindrical shapes with a diameter of 5 mm and a height of 5 mm. These samples underwent biaxial compression testing using an Electronic Universal Testing Machine (Bairoe Instruments, Shanghai, China). A strain rate of 1% of the initial height was applied, and the compression modulus (elastic modulus) was calculated from the recorded strain (%) and stress (MPa).

2.5. Printing Methods and Parameters Optimization.

The printhead was equipped with a 12 Vdc solenoid valve (SMC ITV2050-312l, SMC Company, Tokyo, Japan) for bioink extrusion and connected to this valve through an air tube. The experimental apparatus combined this printhead with a six-degree-of-freedom (6-DOF) UR5 robotic arm with bolts, facilitating the creation of geometric figures and multilayered scaffolds.[44]

Initial experiments focused on optimizing key printing parameters, including air pressure for bioink extrusion and robotic arm velocity, to enhance scaffold structural integrity.[45] In biological 3D printing, controlling these parameters is crucial: air pressure regulates the bioink flow rate and consistency, while printing speed influences the accuracy and quality of the printed structure. Proper adjustment of these factors ensures precise and reliable bioprinting results. A 23G nozzle (inner diameter = 0.34 mm) was selected for bioink extrusion. For the selection of the needle inner diameter, a smaller inner diameter results in a higher shear rate during extrusion. Based on current research on bioprinting, needle diameters ranging from 0.28 to 0.4 mm are the most commonly used.[36,46] This is likely because these needle sizes generate a higher shear rate, reducing the viscosity of the bioink, making extrusion easier, and preventing needle clogging. Therefore, in this study, we chose a 0.34 mm inner diameter needle to be installed on the developed printhead. Additionally, printing on pillars with varied spacings was explored to identify the optimal spacing between strands, which was crucial to prevent the upper layers of multilayer

scaffolds from collapsing, thereby maintaining their structural and functional integrity.[47] The line width and collapse tests were performed five times, with measurements taken using electron microscopy (Guangzhou Xinlun Technology Co., Ltd., Guangzhou, China) for detailed observation. Subsequently, the images were visualized using the S-EYE software (Shenzhen Hayear Electronics Co., Ltd., Shenzhen, China), employing its measurement tools to accurately determine the lengths.

2.6. Printability Assessment.

To comprehensively assess the performance of the developed bioprinter, the experiment utilized the method of printing multilayered biological scaffolds. This approach was selected because the ability to print complex scaffolds accurately reflects the printer's capability in maintaining structural precision and material consistency, essential elements for successful bioprinting.[48,49] The multilayer lattice scaffolds were printed *in situ*, both with and without temperature control. The scaffold printing protocol in this study entailed precooling the GelMA bioink in a refrigerator for an hour, maintaining the bioink at a constant temperature, determined through rheological tests as optimal for GelMA's viscosity, inside the printhead throughout the entire printing process, solidifying scaffolds *via* UV cross-linking layer-by-layer and immediately putting scaffolds into a 37 °C water bath to simulate the temperature environment of the human body (Figure 3). The path of the UR5 robotic arm
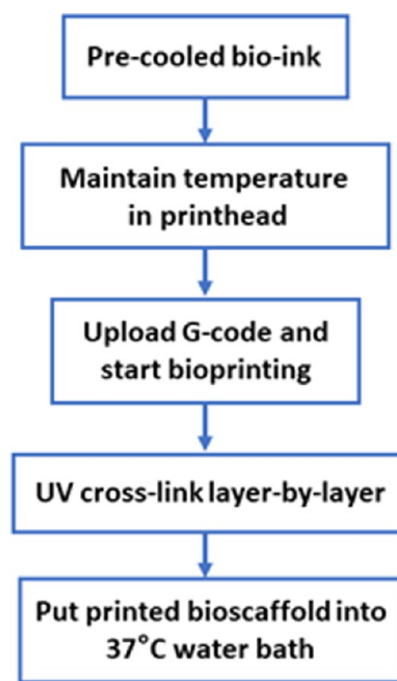
Figure 3. Schematic drawing of the *in situ* bioprinting process.

was programmed using G-code, with the movement speed and extrusion pressure set based on optimization experiments. Pore dimensions of the scaffolds were analyzed using ImageJ, with area measurements conducted under temperature-regulated and unregulated conditions for comparative analysis. Finally, an *in situ* bioprinting test was performed on a defective 3D-printed femur model, the model was obtained from a human CT database in Shanghai Ninth People's Hospital. The pigment-infused GelMA bioink was extruded onto the damaged area of the model.
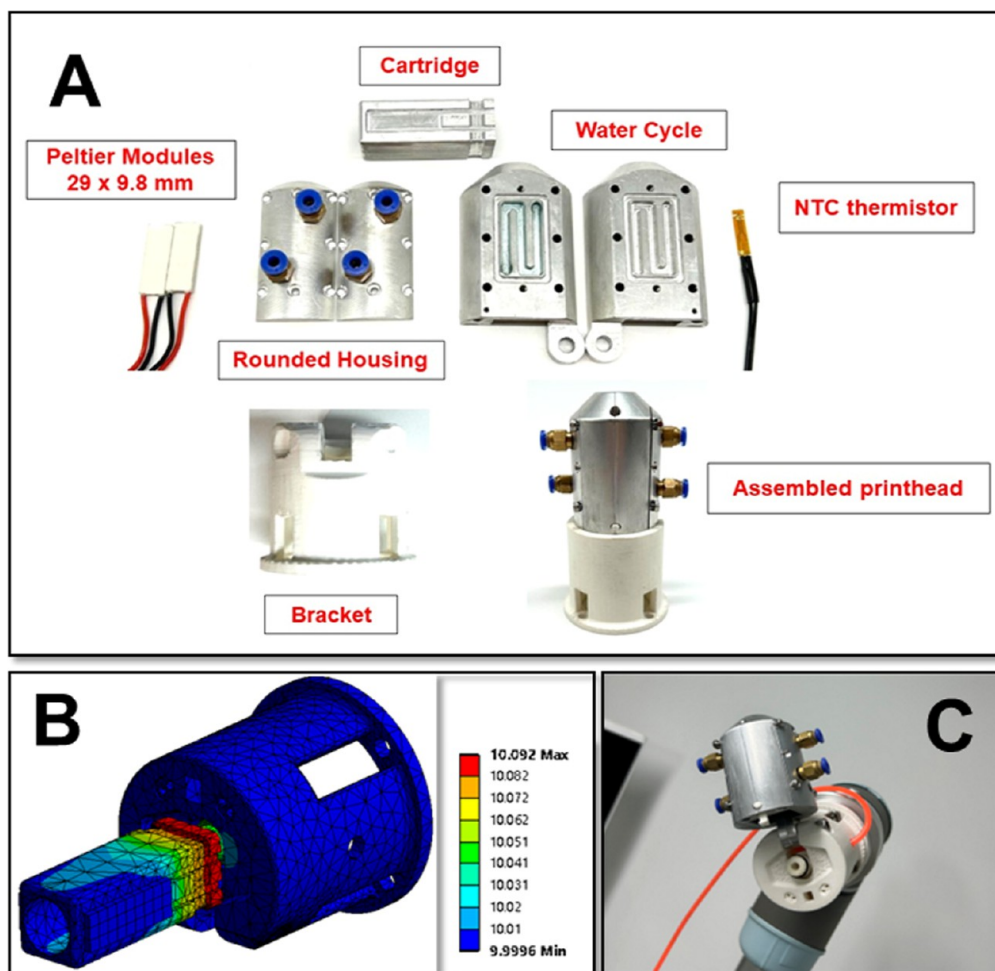
Figure 4. (A) Machined components and assembly of the printhead. (B) The thermal analysis of the printhead. The ambient temperature is set at 22 °C, the Peltier modules were set at 10 °C. The heat transfer shows the maximum temperature is 10.092 °C and the minimum temperature is 9.99 °C. (C) The printhead mounted on the end-effector of UR5.

2.7. Cell Culture and Cell Viability. Cell viability assays were performed on the bioprinted two-layer scaffolds. Rat bone marrow mesenchymal stem cells (rBMSCs) were seeded on these scaffolds and maintained at 37 °C in a 5% CO_2 atm. For the LIVE/DEAD assay, fluorescein isothiocyanate (FITC) and propidium iodide (PI) (Sigma) stains were applied to evaluate cell survival. After the incubation period (7 days), scaffolds were examined under a STELLARIS 8 STED confocal laser scanning microscope (Leica, Germany) at 100× magnification. In this assay, live cells were identified by green fluorescence emitted by FITC, whereas dead cells were marked by the red fluorescence of PI. For the cell counting kit-8 (CCK-8) assay, scaffolds seeded with cells were incubated for 7 days. The CCK-8 solution was respectively added to the culture medium on day 1, day 5, and day 7, followed by a 2 h incubation. Subsequently, a microplate reader measured the absorbance at 450 nm to assess cell proliferation on these specific days. The cell viability rate on the scaffolds was documented. For accuracy, five replicates were performed at each time point.

2.8. Statistical Analysis. Data were expressed as mean ± standard deviation and analyzed using one-way ANOVA for continuous variables. A p-value less than 0.05 was considered to indicate statistical significance.

3. RESULTS

3.1. Printhead Development. All parts of the print head are machined from aluminum alloy. Figure 4A shows printhead components and assembled state diagram. The rounded housing and water cycle plates are fastened with eight bolts and nuts. A cartridge fits into the cylinder formed by the housing and water cycle. To circulate coolant, four male straight fittings on the housing connect to a water pump. Temperature control is achieved by placing two Peltier modules on each side of the cartridge. Within the cartridge, an NTC thermistor is embedded in a groove for temperature monitoring. A flexible articulated hinge links half of the printhead to a 60 mm bracket, enabling versatile positioning. The whole printhead weighs 202 g and measures 82.6 mm in length. Figure 4C shows the actual printhead assembly mounted on the UR5 robotic arm. A steady-state thermal analysis was conducted in ANSYS Workbench: the printhead model was segmented into 96,000 nodes, with ambient temperatures set at 22 °C and Peltier modules adjusted to maintain a temperature of 10 °C. This analysis concentrated on the heat transfer processes from the Peltier modules to the bioink cartridges. The analysis results, illustrated in Figure 4B, reveal a minimal internal temperature differential within the printhead at 10 °C, solidly supporting the printhead's ability to
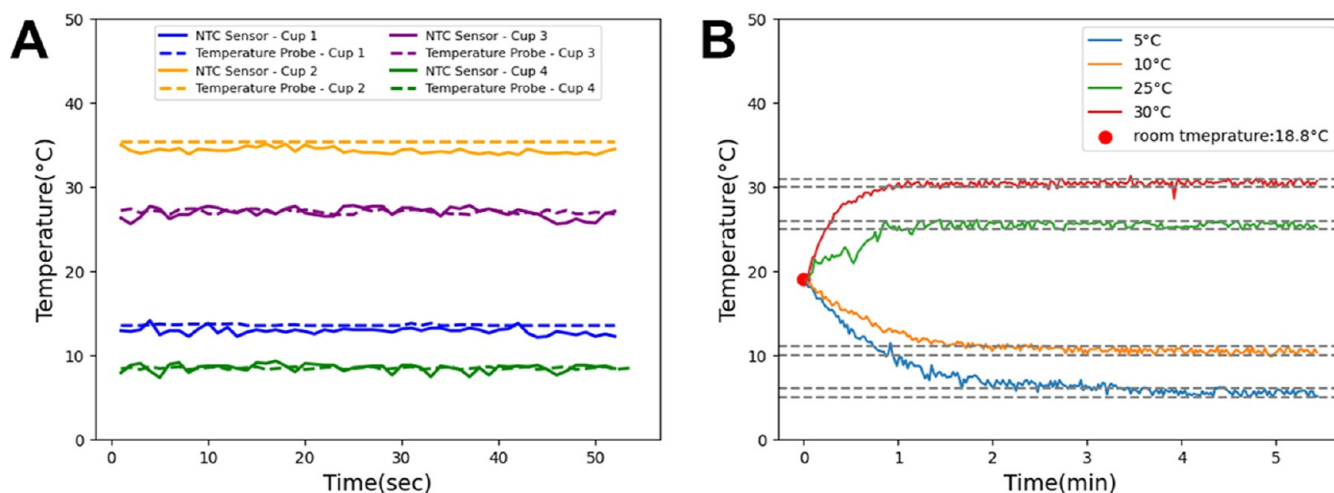
Figure 5. (A) The NTC thermistor was calibrated using a temperature probe to verify its temperature data collection accuracy. Both sensors measured temperatures in four cups of water, each at varying temperatures, over 1 min. (B) The target temperature's numerical fluctuations and the response time. Room temperature, initially at 18.8 °C, increased to 25 and 30 °C, then decreased to 5 and 10 °C. Two gray dotted lines form the stabilization patterns.

maintain optimal performance temperatures, crucial for high-quality bioprinting applications.

3.2. Temperature Control Performance. The printhead's heating and cooling efficiency was assessed. By inputting the desired temperatures *via* the serial port interface, we could monitor in real time the ambient temperature changes on the bioink inside the printhead. Figure 5A presents the temperature discrepancies measured by the NTC thermistor compared to a probe in four separate glasses of water at different temperatures. The data revealed a maximum error of 1 °C at elevated temperatures but otherwise exhibited close agreement, validating the NTC's precision in real-time temperature monitoring. Figure 5B illustrates the performance of a temperature control system under PID algorithm. Target temperatures were input *via* the serial port interface, triggering the STM32 to control the Peltier modules for heating/cooling. Real-time temperature values were then accurately recorded *via* the NTC. The room temperature (18.8 °C) increased to 25 and 30 °C and subsequently decreased to 5 and 10 °C. The results showed that heating is notably more rapid than cooling, requiring less than a minute to reach 25 and 30 °C. In contrast, cooling to 10 °C took approximately 2.7 min, and stabilizing just above 5 °C nearly 3.5 min. The gray dotted line indicated the temperature errors (ranging from +0.1 to 1 °C) when readings stabilized. Additionally, Table 1 detailing the control system's response times for both heating and cooling at various initial temperatures was analyzed. It was observed that cooling times for Peltier modules from 30 °C, in 5 °C intervals, exhibited a gradual increase in response time. Conversely, when the temperature was incrementally raised from 5 °C in 5 °C steps, the response time remained more consistent. The printhead's temperature control accuracy was observed to be relatively ideal, with future improvements aimed at reducing the cooling time to approximately 1 min.

3.3. Rheology and Mechanical Properties of GelMA. Formulations were chosen with GelMA concentrations ranging from 5% to 15% and LAP concentrations from 0.25% to 0.75% due to their temperature-sensitive rheological properties. As shown in Figure 6A, the GelMA demonstrates a significant increase in viscosity as temperature decreases from 15 to 5 °C, ensuring enhanced control over bioink flow during printing.

Table 1. Response Time of Using Printhead's Temperature-Regulated System to Heat up and Cool Down in Five Incremental Steps Respectively

operating mode	starting temperature (°C)	target temperature (°C)	response time (S)
cooling	30	25	39
	25	20	79
	20	15	87
	15	10	115
	10	5	216
heating	5	10	6
	10	15	22
	15	20	33
	20	25	36
	25	30	34

Figure 6B illustrates the transition of GelMA's storage and loss modulus with temperature, showcasing its adaptability from a solid-like glassy state to a more fluid-like rubbery and flow state. A constant shear rate in Figure 7A,B is of 1 s^{-1}. Higher concentrations of GelMA lead to increased viscosity and higher storage and loss modulus while varying LAP ratios do not significantly affect these rheological properties. Additionally, Figure 6C,D illustrate the mechanical properties of the bioink. Compression tests on cylindrical samples using an electronic universal testing machine revealed that the elastic modulus of GelMA + LAP mixtures remained stable despite changes in LAP concentration. However, higher concentrations of GelMA improved the structural stability and load-bearing capacity of the samples.

3.4. Printing Parameters Optimization. To determine the optimal printing parameters for GelMA scaffolds, a series of experiments were conducted at 5 °C to maintain an ideal viscosity as indicated by the viscosity-temperature curve presented in Figure 6A. From Figure 7A, the printing process involved extruding GelMA through a 23G nozzle onto a smooth substrate. It was noted that the formation of coherent strands was unachievable at air pressures below 0.04 MPa and speeds exceeding 15 mm/s.
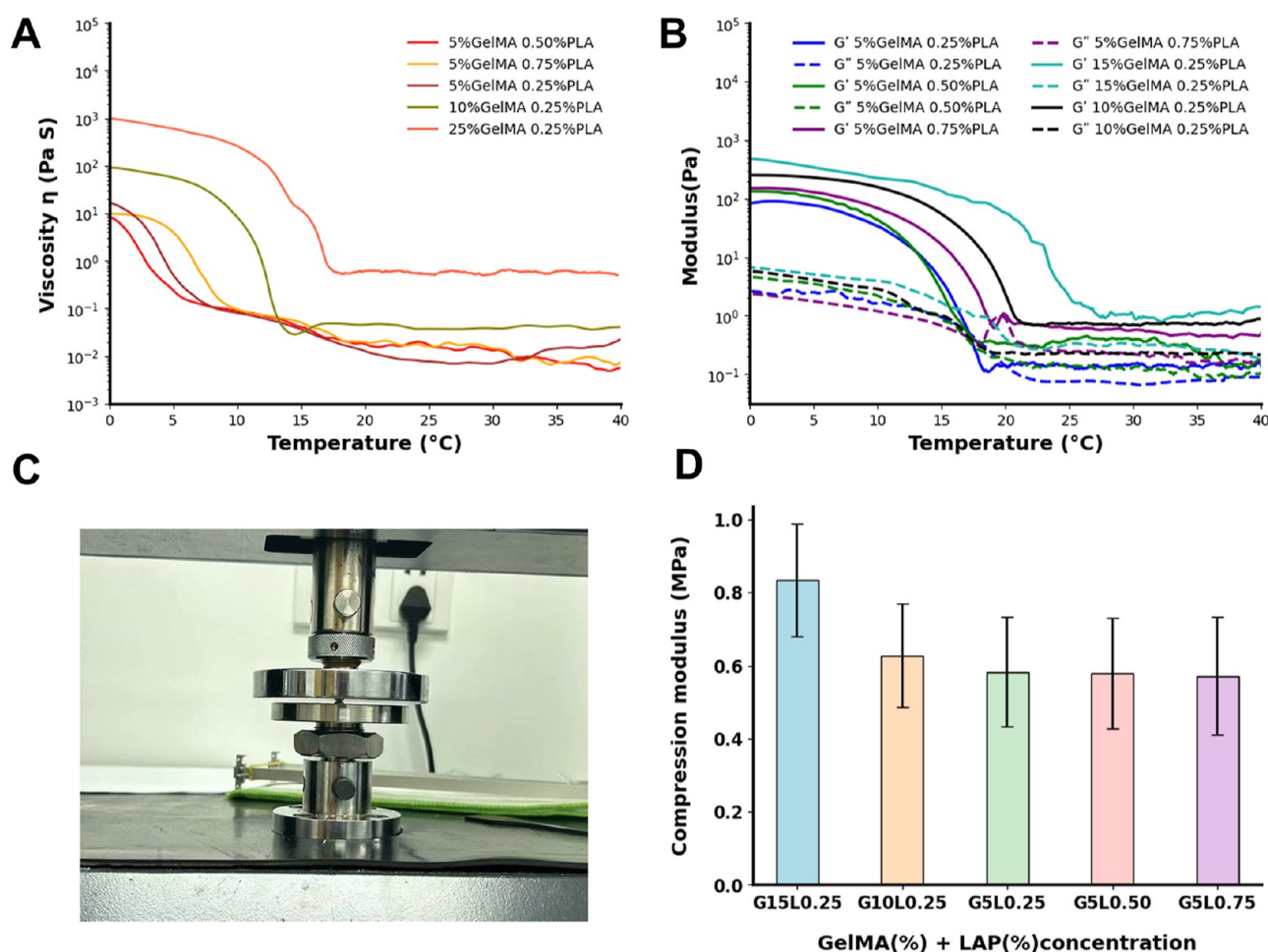
Figure 6. Rheology and mechanical properties of 5, 10, 15% (w/v) GelMA + 0.25, 0.50, 0.75% (w/v) LAP based hydrogels. (abbreviated G5L0.25) (A) Viscosity-temperature curve. (B) Storage and loss moduli-temperature curve. (C) Typical illustration of the hydrogel specimen during a compression test. (D) Compression modulus of the hydrogel samples printed at varying concentrations of GelMA and LAP.

In the initial experimental phase, with a constant robotic arm speed of 11 mm/s, the air pressure was in increments of 0.01 MPa from 0.04 to 0.09 MPa. Subsequently, with the air pressure fixed at 0.06 MPa, the arm's speed was adjusted across a range from 5 to 15 mm/s in increments of 2 mm/s. The resulting strand appearances, visualized using electron microscopy, are illustrated in Figure 7B,C. These images corroborate that increased air pressure leads to wider strands, while increased movement speeds result in narrower strands.

The quantitative outcomes of these manipulations are graphically summarized in Figure 7D,E, where statistical analyses of line widths are presented across varying air pressures and movement speeds. This analysis was specifically conducted to determine the optimal settings of air pressure and moving speed for the subsequent printing of bioscaffolds. We aimed to ensure that the filament dimensions closely match those of the nozzle, thereby minimizing any variability that could affect the pore size measurements of the printed bioscaffolds. A direct correlation was observed: as air pressure increased or speed decreased, the width of the GelMA strands also increased. Taking into account the 0.34 mm inner diameter of our nozzle, the optimal printing parameters for follow-up multilayer scaffold printing were determined to be around 0.06 MPa for air pressure and 11 mm/s for the movement speed, where the produced strand widths closely matched the nozzle's inner diameter. Figure 8A shows the

effect images of varying spacing on pillar stability in collapse printing tests, with each pillar standing 6 mm tall and spacings incrementing from 1 to 6 mm. Figure 8B measures the distance from the lowest point of the collapsed strand to the horizontal plane under different printing parameters using electron microscopy. Theoretically, a collapse distance closer to 6 indicates a lower degree of strand collapse, thus determining the best spacing for each line when printing this GelMA scaffold. Figure 8C,D demonstrate the distances of strand collapse under different printing parameters, revealing that the most significant collapses—and those most affected by printing parameters—occurred at spacings 5 and 6. The trends of collapse at other spacings were relatively flat and values were similar, around 5.5 mm. Therefore, in subsequent experiments for printing 3D scaffolds, the grid width was set at 3 mm per cell.

3.5. Bioprinting Multilayer Bioscaffolds. The "stackability" of the printhead was evaluated using UR5 to *in situ* print multilayer lattice scaffolds. The printing pathway was designed using CAD software (SolidWorks), followed by slicing the STL files to generate distinct G-codes on ideaMaker (Raise3D). These codes were then uploaded to the UR5 robotic arm for execution. Initially, precooled GelMA was printed on Petri dishes to form a lattice scaffold without temperature regulation. Subsequently, we activated the printhead's cooling system to maintain the bioink's ambient
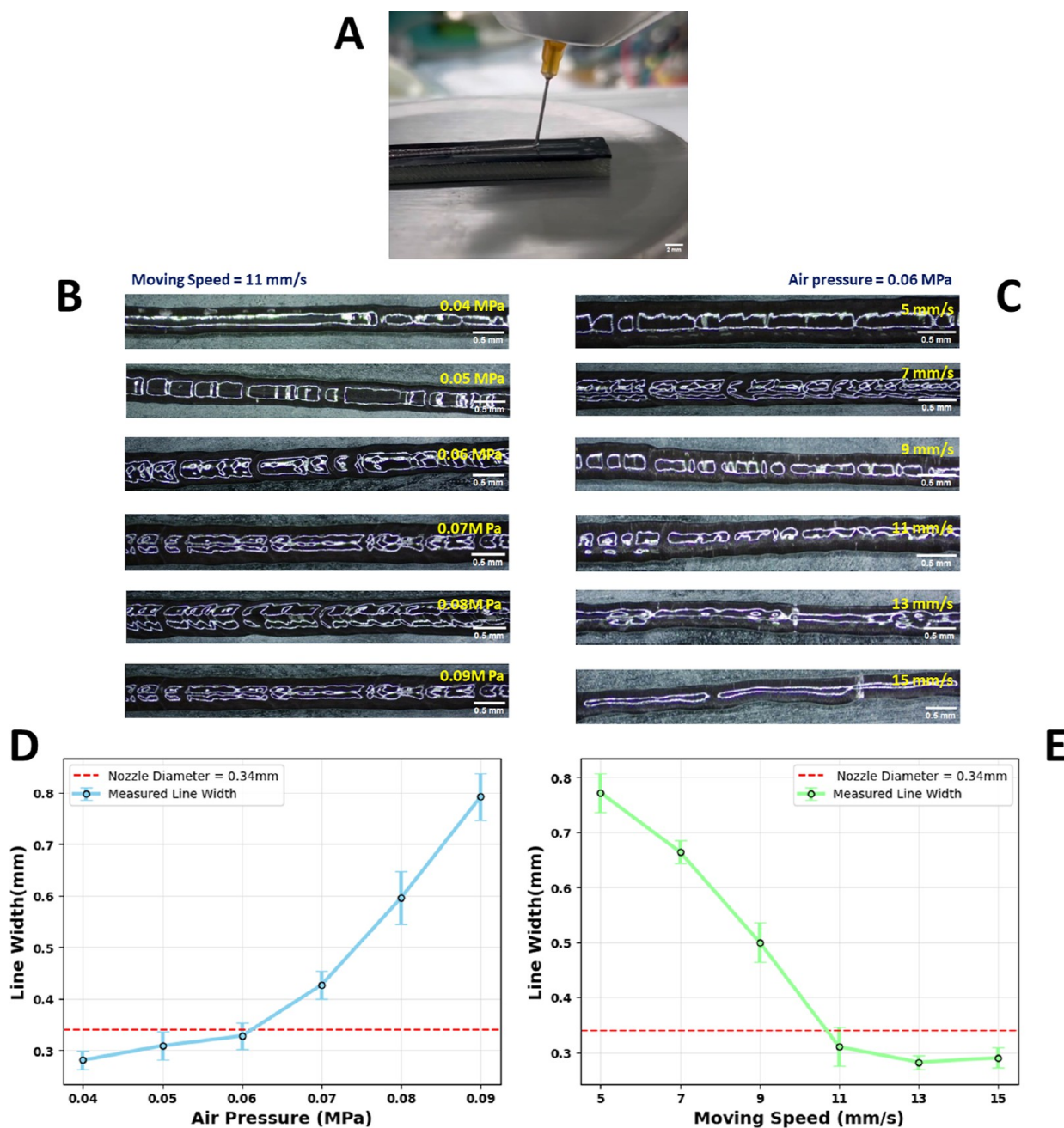
Figure 7. (A) Specifying a range of air pressure and robotic arm's moving speed through printing strands on a platform. (Scale bar: 2 mm) (B,C) Strands printed at varied air pressures and the robotic arm's moving speed, screened by electron microscopy. (Scale bar: 0.5 mm) (D) Line width (mm) increases with air pressures from 0.04 to 0.09 MPa. (E) Decreasing line width (mm) with increasing moving speeds from 5 to 15 mm/s. ($n = 5$ independent samples).

temperature at approximately 5 °C, thereby reprinting the scaffolds. The temperature of 5 °C was selected based on the viscosity-temperature curve from rheological testing. This choice was due to lower temperatures requiring longer cooling times, which would extend the experiment duration. Based on the experimental results from Section 3.4, the air pressure for bioink extrusion was set to 0.06 MPa, and the robotic arm's printing speed was established at 11 mm/s. The initial grid spacing, set at 3 mm based on collapse test results, was increased to 5 mm to account for the widening line widths as scaffold layers multiplied. This modification resulted in a scaffold comprising nine lattices, each 15×15 mm^2. Figure 9A shows the bioprinting process on the Petri dish. Figure 9B,C

shows the printed 2-layer 15×15 mm^2 scaffold. A 405 nm UV light model UVLD8 (Shenzhen Guanghuashi Technology Co., Ltd., Shenzhen, China), with an 8 mm diameter speckle size, is used for layer-by-layer photo-cross-linking, followed by imaging *via* electron microscopy. Photocuring accompanied the entire printing process. The UV light was turned on as soon as the bioink extrusion began to form filaments and remained on until the printing process was complete. To safeguard the Petri dishes from UV light exposure, we covered the dishes with Teflon high-temperature insulation cloth.

As shown in Figure 10A, photographs of 2-layer, 5-layer, and 8-layer scaffolds printed under temperature control (5 °C) and without temperature control were captured using an electron
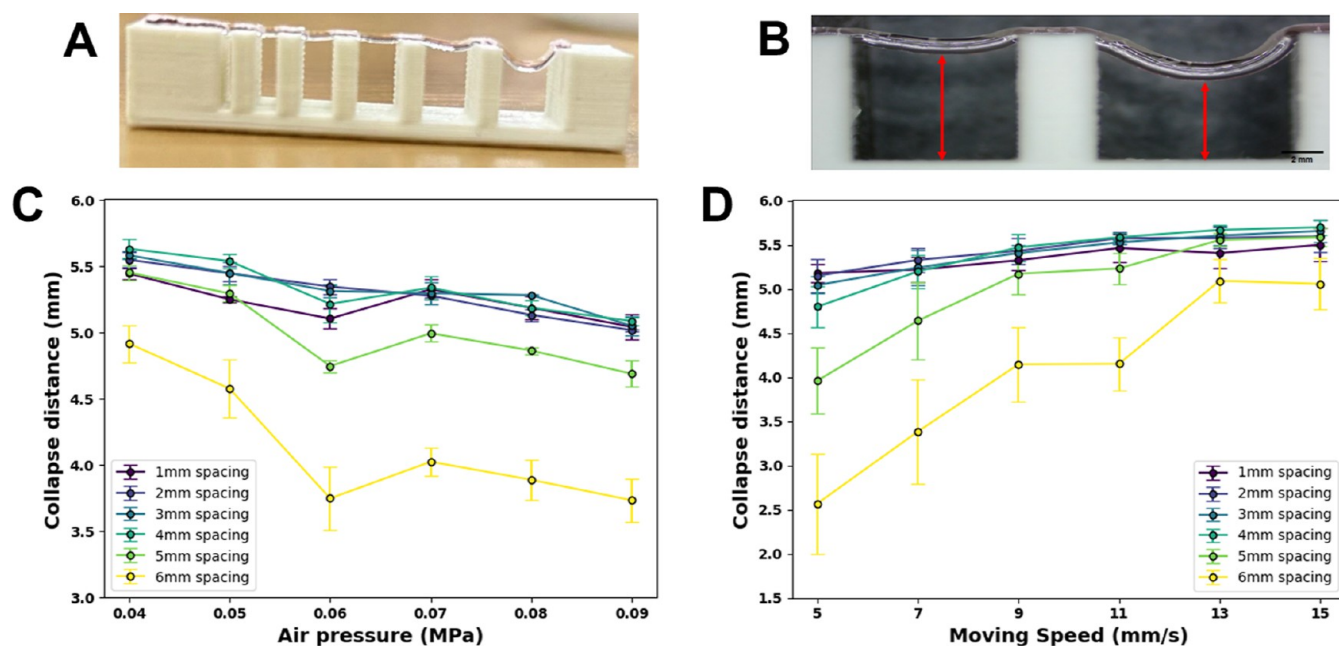
Figure 8. (A) Specifying the spacing of the bioscaffold through printing strands on pillars with varying spacings under 5 °C. (B) Calculating the strand's collapse distances. (Scale bar: 2 mm) (C,D) Collapse distances for bioscaffold strands at air pressures and moving speeds, across 1−6 mm spacings. (n = 5 independent samples).
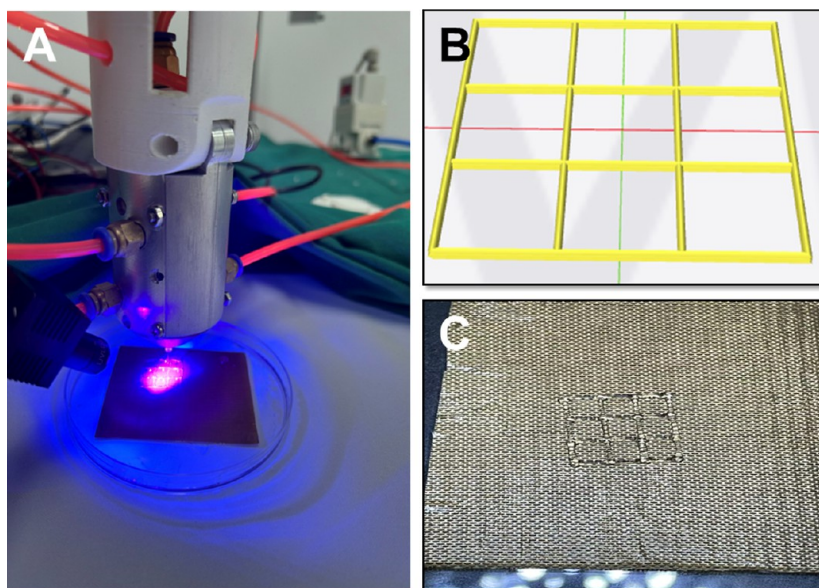

Figure 9. (A) *in situ* bioprinting scaffolds on a Petri dish. (B) The scaffold model with certain layers. (C) The printed 2-layer GelMA scaffold after UV cross-linking.

microscope. It can be observed that the scaffolds have a more complete and uniform structure under temperature control. Without temperature regulation, the increased number of layers and extended printing time reduced the viscosity of precooled GelMA, causing it to liquefy upon long-term exposure to ambient temperature. Figure 10B presents a comparison of pore area measurements conducted on each grid using ImageJ software, clearly demonstrating a trend of decreasing pore area with an increasing number of layers. The 2-layer scaffolds were immediately placed in a 37 °C water bath after printing to simulate a real human scenario. Observations were made at 0, 24, and 72 h. Figure 11A shows that the lattice structure stretched over time in the water

bath. Figure 11B,C demonstrate changes in line width and pore size. Despite these changes, Figure 11A,D reveal that the 2-layer structure maintains high shape fidelity, clear contours, and favorable mechanical properties, allowing it to be picked with tweezers.

A preliminary *in situ* bioprinting test on a defective femur model is presented in Figure 12 presents. This model was previously converted into STL format *via* CT scanning and has been 3D printed (Figure 12A). The defective area (diameter 8 mm, depth 3 mm) was sliced into a G-code file to establish the printing path (Figure 12B). Throughout the printing process, the printhead temperature was maintained at 5 °C. As depicted in Figure 12C, the printed scaffolds filled the entire defect on
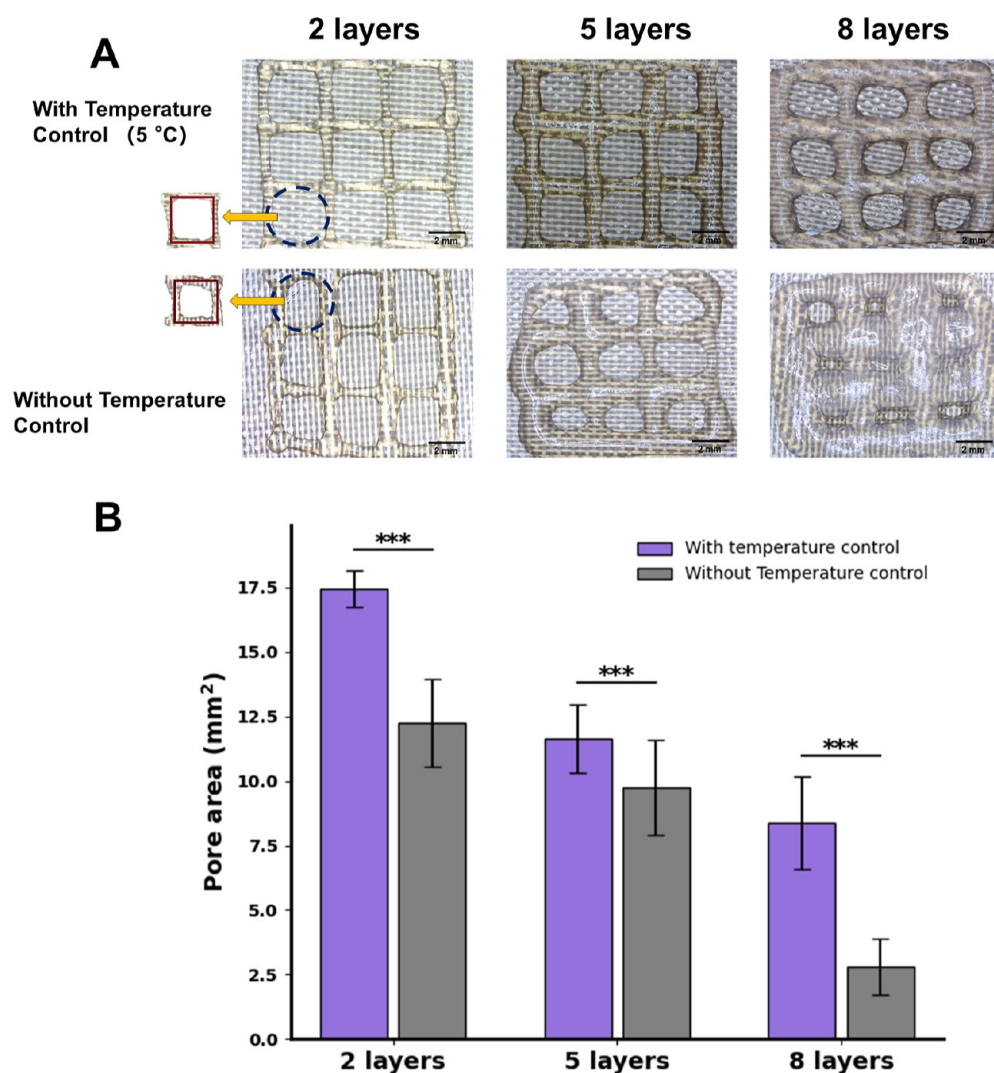
Figure 10. Structural comparison of scaffolds with different layer counts. (A) Printing results of 2-layer, 5-layer, and 8-layer scaffolds with temperature control (5 °C) and without temperature control. (Scale bar: 2 mm) (B) Comparison of pore area quantified using ImageJ software. Data are presented as mean ± standard deviation. The results indicate the printhead's exceptional temperature control capabilities. ($n = 5$ independent tests) (***: $P < 0.001$).

the femur model, with most of the printed outcomes being filamentous and not merging into a single blur. However, the relatively small area may limit clear observation, particularly due to its size and depth, which affects the visibility of the scaffold's "stackability" from a side view. Future *in situ* bioprinting tests should be conducted on a larger area with shallow depth.

3.6. Cell Viability. LIVE/DEAD assay outcomes for a bioprinted two-layer scaffold are shown in Figure 13A, using a STELLARIS 8 STED confocal laser scanning microscope. Live/dead cells were stained using the Calcein-AM/PI (Beyotime Biotechnology, Shanghai, China) staining kit as cell dyes. CoImages are categorized into live (green), dead (red), and merge sections, demonstrating predominant cell viability after 5 and 7 days of culture. However, we could not capture clear imaging of cross-shaped scaffolds due to the confocal microscope's minimum 10× magnification limit; conversely, utilizing a lower magnification microscope enables distinct visualization of these structures, albeit compromising the clarity of cellular morphology. Figure 13B illustrates cell viability trends *via* CCK-8 assays. Initial viability peaks near

100% on day 1, with a slight decrease by days 5 and 7, yet viability remains high, indicating sustained cell health. This slight reduction in viability may stem from limited pore size (5 × 5 mm^2) and lattice number (nine), we speculate that increasing the number of lattices may expand the cell attachment area, thereby enhancing cell viability. Overall, cell viability proved relatively consistent, suggesting that the scaffolds printed with a temperature-regulated printhead support effective cell growth and survival.

4. DISCUSSION

This study has developed a temperature-regulated printhead for robot-assisted *in situ* bioprinting, enhancing the precision of printing with thermosensitive bioinks, and maintaining cellular activity to a certain degree. By incorporating an advanced temperature control system, it ensures the bioink maintains optimal viscosity throughout the printing process, leading to high-resolution bioprinted scaffolds.

Despite recent advancements in robot-assisted *in situ* bioprinting technology, most current studies have concentrated on optimizing the robot's printing path planning,[50,51]
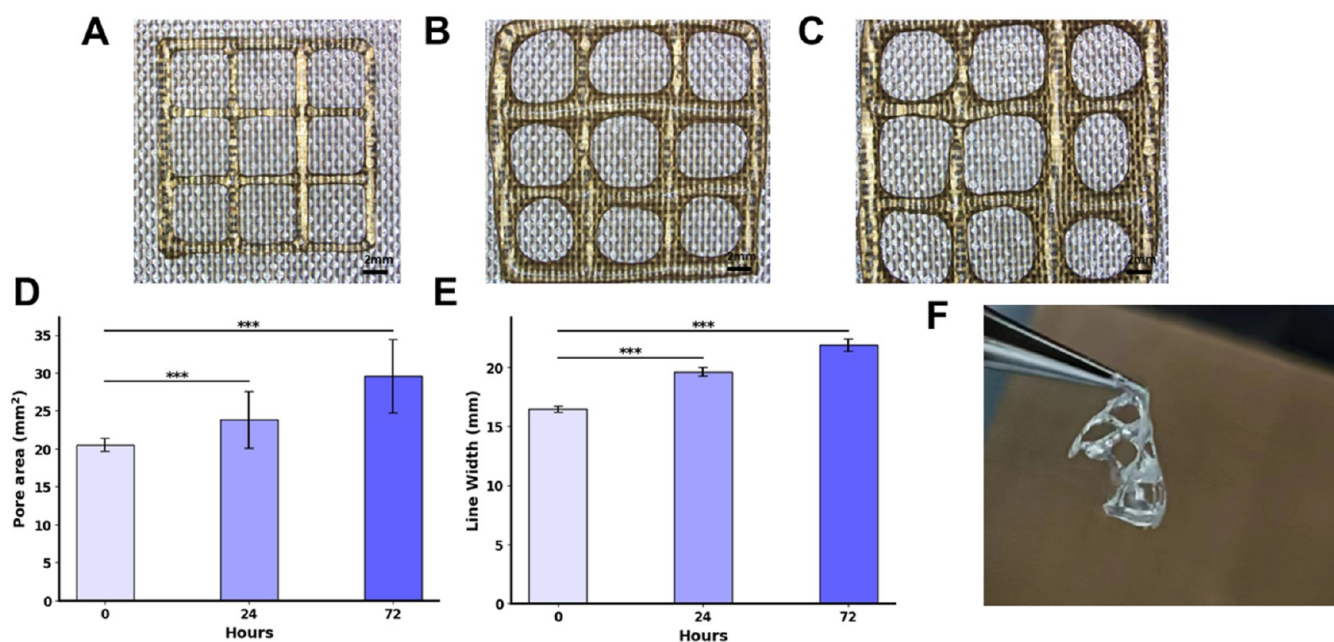
Figure 11. (A) The same 2-layer scaffold after being placed in a 37 °C water bath for 0, 24, and 72 h. (B,C) The quantified results of the scaffold's line width and pore area changes over time in a 37 °C water bath. (Scale bar: 2 mm) Data are presented as mean ± standard deviation. (D) The scaffold has favorable mechanical properties, allowing it to be picked up with tweezers. (n = 5 independent tests) (***: $P < 0.001$).
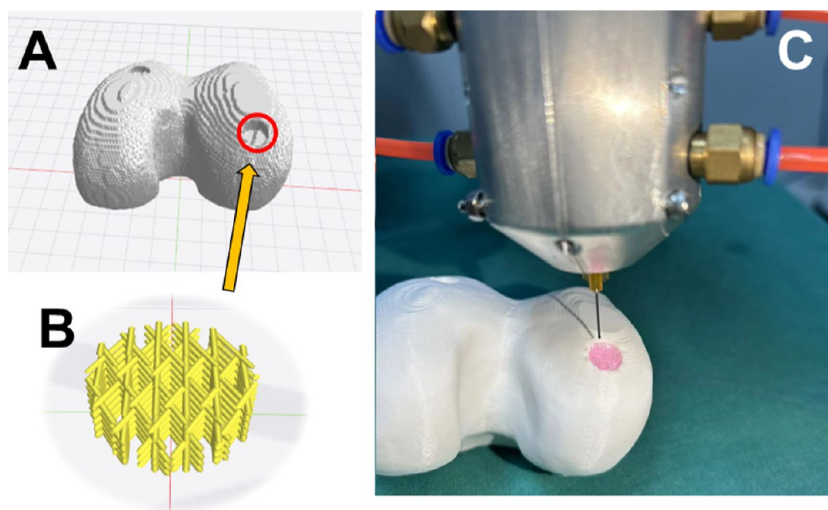

Figure 12. (A) An STL format femur model, highlighting a defect area circled in red. (B) G-code paths for bioprinting a scaffold, generated from slicing the defect. (C) *In situ* bioprinting on the femur model: employing a temperature-regulated printhead mounted on a UR5 robot to extrude GelMA onto the defect.

often overlooking the necessity to control the physical properties of thermosensitive materials commonly used in this field. As the viscosity of bioinks can vary significantly, becoming either too thick or too liquid when printed at room temperature, there arises a critical need for temperature regulation. Addressing this issue, the printhead presented in this study introduces an innovative solution that precisely controls the temperature of the bioink, thereby significantly improving the printing process.

In terms of technological innovation, one of the key novelties of the temperature-regulated printhead is its uniquely designed S-shaped water-cooling plate, which significantly enhances cooling efficiency. This design allows for direct heat dissipation, eliminating the need for external fans or temperature control enclosures that increase the size and complexity

of installation in conventional bioprinters. However, it has been observed that as the number of layers in the bioprinted scaffold increases (Figure 10), the gaps between the strands gradually narrow. Regardless of whether temperature control is used, the pore size of higher-level scaffolds tends to decrease. This phenomenon may be attributed to the pressure from the upper layers causing the lower layers to collapse, thereby reducing the pore size. Therefore, while temperature control significantly improves the print quality of the initial layers, its impact diminishes when printing multilayered structures. Future research should focus on improving the structural support capability of multilayered scaffolds. On the other hand, while the structure of the printed 2-layer scaffold stretched after prolonged exposure to the 37 °C water bath, the mechanical integrity remained strong and complete despite the
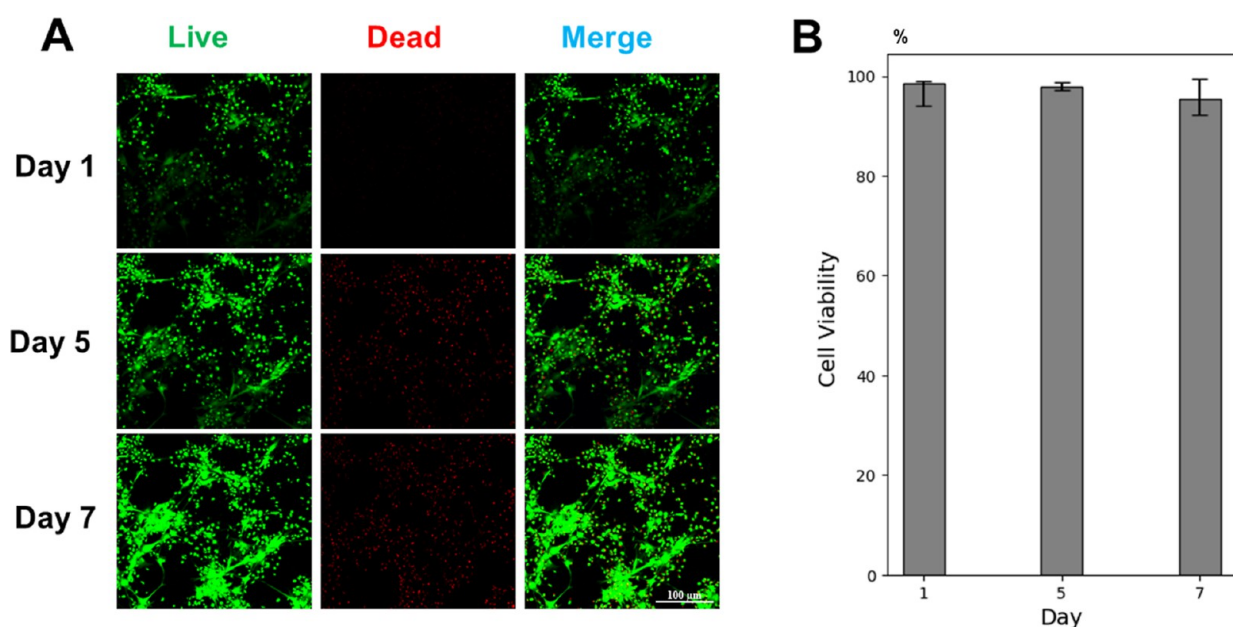
Figure 13. Cell viability assay of 7 days culture in printed 2-layer GelMA scaffold. (A) Live/Dead test shows fluorescent staining of live (green) and dead (red) cells at different time points (day 1, day 5, day 7). (B) The CCK-8 assay shows a minor decrease in cell viability, but overall rates remain high, indicating strong cell health. (Scale bars: 100 μm).

overall lattice size increasing. This demonstrates that the printed GelMA scaffold can maintain structural integrity *in vivo*.

Moreover, the design of the photopolymerization device remains a critical focus for the quality of the formed bioprinted scaffolds.[52,53] In clinical settings, the printing and photo-cross-linking processes of bioink should occur simultaneously, particularly when performing *in situ* bioprinting directly on human or animal skin. Thus, it is vital to ensure that the photopolymerization device can effectively cross-link the bioink during the printing process while avoiding harm to surrounding healthy tissues or cells. However, this study employed a method where UV light was used for additional curing postprinting, which may be impractical in clinical applications. Considering the focus of this research is the development of a temperature-regulated printhead for robot-assisted *in situ* bioprinting, future endeavors should involve refining the photopolymerization device and bioink formulation to meet the *in situ* printing demands and conditions in clinical environments.

5. CONCLUSION

In this study, we introduce a compact, temperature-regulated printhead designed to improve thermosensitive bioink performance for bioscaffold fabrication in robot-assisted *in situ* bioprinting. We have designed and fabricated the printhead with machined parts and electronic components. Utilizing UR5 robotic arm assistance, the bioprinted multilayered scaffolds with GelMA bioink under certain temperature settings showed good integrity. Further, the enhanced cell viability and proliferation evidenced by LIVE/DEAD assays and CCK-8 tests underpin the printhead's potential to produce viable, functional tissue constructs. Ultimately, our findings underscore the pivotal role of temperature control in optimizing the performance of temperature-sensitive bioinks like GelMA, thereby facilitating advanced *in situ* bioprinting strategies for tissue engineering and regenerative medicine.

Future work should address these limitations: (1) bioink capacity is limited to 5 mL due to device miniaturization, causing potential material shortages during bioprinting. Solutions for midprocess syringe refilling are needed. (2) The suitability of current GelMA for subcutaneous tissue reconstruction is uncertain due to challenges in internal bioink cross-linking. The development of new materials that combine strong mechanical properties with enhanced cell viability is necessary. (3) The printhead's cooling function is less efficient than its heating capability. Enhancements in the cooling system, possibly through updated Peltier modules or PID algorithms, are required. (4) Conducting *in situ* bioprinting experiments on models with large, damaged areas and shallow depth, such as wounded skin, as well as on actual animals.

■ ASSOCIATED CONTENT

ⓢ Supporting Information

The Supporting Information is available free of charge at https://pubs.acs.org/doi/10.1021/acsomega.4c04373.

> 2D engineering drawings and components: fabrication 2D drawings. Stm32 PID & NTC: temperature sensing and PID code. Assembly: the bracket's model (ZIP)

■ AUTHOR INFORMATION

Corresponding Author

Jinwu Wang — *Shanghai Ninth People's Hospital, School of Medicine, Shanghai Jiao Tong University, Shanghai 200011, China;* ⓞ orcid.org/0000-0001-6569-6991; Email: wangjw-team@shsmu.edu.cn

Authors

Zitong Wang — *Department of Biomedical Engineering, School of Health Science and Engineering, University of Shanghai for Science and Technology, Shanghai 200093, China*

Li Lin — *Shanghai Ninth People's Hospital, School of Medicine, Shanghai Jiao Tong University, Shanghai 200011, China*

Xiangyu Li − *Department of Mechanical, School of Mechanical & Electrical Engineering, Henan University of Technology, Zhengzhou 450001 Henan Province, China*

Quan Zhang − *School of Pharmacy, Jiangsu Ocean University, Lianyungang 222005 Jiangsu Province, China*

Xuelian Mi − *Institute of Biomedical Engineering, College of Medicine, Southwest Jiaotong University, Chengdu 611756 Sichuan Province, China*

Bide Xu − *Innovative Medical Device Registration Research and Clinical Transformation Service Center, Institute of Translational Medicine, Shanghai Jiao Tong University, Shanghai 200240, China*

Yuanjing Xu − *Department of Biomedical Instrument, Institute of Translational Medicine, Shanghai Jiao Tong University, Shanghai 200240, China*

Tongyou Liu − *Department of Biomedical Instrument, Institute of Translational Medicine, Shanghai Jiao Tong University, Shanghai 200240, China*

Yuling Shen − *School of Future Science and Engineering, Soochow University, Soochow 215021 Jiangsu Province, China*

Zan Wang − *Department of Mechanical, School of Mechanical & Electrical Engineering, Henan University of Technology, Zhengzhou 450001 Henan Province, China*

Neng Xie − *Department of Biomedical Manufacturing and Engineering, School of Mechanical Engineering, Shanghai Jiao Tong University, Shanghai 200011, China*

Complete contact information is available at:
https://pubs.acs.org/10.1021/acsomega.4c04373

Author Contributions

Zitong W. and Y.S.: Writing—original draft, review and edit. Zitong W., X.L. and T.L.: Methodology. Zitong W., Q.Z. and X.M.: Validation and Formal analysis. L.L. and B.X.: Investigation. L.L., Y.X. and B.X.: Conceptualization. L.L., Y.X., Zan W., N.X. and J.W.: Supervision. L.L., N.X. and J.W.: Funding acquisition.

Notes

The authors declare no competing financial interest.

■ ACKNOWLEDGMENTS

■ REFERENCES

(1) Hong, N.; Yang, G. H.; Lee, J.; Kim, G. 3D bioprinting and its in vivo applications. *J. Biomed. Mater. Res. B Appl. Biomater.* **2018**, *106* (1), 444−459.

(2) Han, J.; Kim, D. S.; Jang, H.; Kim, H. R.; Kang, H. W. Bioprinting of three-dimensional dentin−pulp complex with local differentiation of human dental pulp stem cells. *J. Tissue Eng.* **2019**, *10*, 204173141984584.

(3) Murphy, S. V.; De Coppi, P.; Atala, A. Opportunities and challenges of translational 3D bioprinting. *Nat. Biomed. Eng.* **2020**, *4*, 370−380.

(4) Sun, W.; Starly, B.; Daly, A. C.; Burdick, J. A.; Groll, J.; Skeldon, G.; Shu, W.; Sakai, Y.; Shinohara, M.; Nishikawa, M.; Jang, J.; et al. The bioprinting roadmap. *Biofabrication* **2020**, *12*, 022002.

(5) Kačarević, Ž. P.; Rider, P. M.; Alkildani, S.; Retnasingh, S.; Smeets, R.; Jung, O.; Ivanišević, Z.; Barbeck, M. An introduction to 3D bioprinting: possibilities, challenges and future aspects. *Materials* **2018**, *11* (11), 2199.

(6) Manita, P. G.; Garcia-Orue, I.; Santos-Vizcaino, E.; Hernandez, R. M.; Igartua, M. 3D bioprinting of functional skin substitutes: From current achievements to future goals. *Pharmaceuticals* **2021**, *14* (4), 362.

(7) Liu, N.; Ye, X.; Yao, B.; Zhao, M.; Wu, P.; Liu, G.; Zhuang, D.; Jiang, H.; Chen, X.; He, Y.; Huang, S.; et al. Advances in 3D bioprinting technology for cardiac tissue engineering and regeneration. *Bioact. Mater.* **2021**, *6* (5), 1388−1401.

(8) Jafari, A.; Ajji, Z.; Mousavi, A.; Naghieh, S.; Bencherif, S. A.; Savoji, H. Latest advances in 3D bioprinting of cardiac tissues. *Adv. Mater. Technol.* **2022**, *7* (11), 2101636.

(9) Cadena, M.; Ning, L.; King, A.; Hwang, B.; Jin, L.; Serpooshan, V.; Sloan, S. A. 3D bioprinting of neural tissues. *Adv. Healthcare Mater.* **2021**, *10* (15), 2001600.

(10) Daikuara, L. Y.; Chen, X.; Yue, Z.; Skropeta, D.; Wood, F. M.; Fear, M. W.; Wallace, G. G. 3D bioprinting constructs to facilitate skin regeneration. *Adv. Funct. Mater.* **2022**, *32*, 2105080.

(11) Iberite, F.; Badiola-Mateos, M.; Loggini, S.; Paci, C.; Ruspi, J.; Iachetta, D.; Mannini, A.; Gruppioni, E.; Ricotti, L. 3D bioprinting of thermosensitive inks based on gelatin, hyaluronic acid, and fibrinogen: Reproducibility and role of printing parameters. *Bioprinting* **2024**, *39*, No. e00338.

(12) Erdem, A.; Darabi, M. A.; Nasiri, R.; Sangabathuni, S.; Ertas, Y. N.; Alem, H.; Hosseini, V.; Shamloo, A.; Nasr, A. S.; Ahadian, S.; Dokmeci, M. R.; et al. 3D bioprinting of oxygenated cell-laden gelatin methacryloyl constructs. *Adv. Healthcare Mater.* **2020**, *9* (15), 1901794.

(13) Hibbert, M.; Viljoen, J. M.; du Plessis, L. H. Print parameter optimisation for a Pluronic F-127 and alginate hybrid hydrogel. *Bioprinting* **2023**, *30*, No. e00257.

(14) Xie, N.; Shi, G.; Shen, Y.; Xu, Y.; Wang, H.; Feng, H.; Dai, K.; Wang, J.; Cao, Q. Research progress of robot technology in in situ 3D bioprinting. *Int. J. Bioprint.* **2022**, *8* (4), 614.

(15) Wang, M.; He, J.; Liu, Y.; Li, M.; Li, D.; Jin, Z. The trend towards in vivo bioprinting. *Int. J. Bioprint.* **2015**, *1* (1), 15.

(16) Ashammakhi, N.; Ahadian, S.; Pountos, I.; Hu, S. K.; Tellisi, N.; Bandaru, P.; Ostrovidov, S.; Dokmeci, M. R.; Khademhosseini, A. In situ three-dimensional printing for reparative and regenerative therapy. *Biomed. Microdevices* **2019**, *21*, 42.

(17) Dias, J. R.; Ribeiro, N.; Baptista-Silva, S.; Costa-Pinto, A. R.; Alves, N.; Oliveira, A. L. In situ enabling approaches for tissue regeneration: Current challenges and new developments. *Front. Bioeng. Biotechnol.* **2020**, *8*, 85.

(18) Wang, Z.; Liang, X.; Wang, G.; Wang, X.; Chen, Y. Emerging bioprinting for wound healing. *Adv. Mater.* **2023**, 2304738.

(19) Dong, H.; Hu, B.; Zhang, W.; Xie, W.; Mo, J.; Sun, H.; Shang, J. Robotic-assisted automated in situ bioprinting. *Int. J. Bioprint.* **2023**, *9* (1), 629.

(20) Pazhouhnia, Z.; Beheshtizadeh, N.; Namini, M. S.; Lotfibakhshaiesh, N. Portable hand-held bioprinters promote in situ tissue regeneration. *Bioeng. Transl. Med.* **2022**, *7* (3), No. e10307.

(21) Ying, G.; Manríquez, J.; Wu, D.; Zhang, J.; Jiang, N.; Maharjan, S.; Hernández Medina, D.; Zhang, Y. S. An open-source handheld extruder loaded with pore-forming bioink for in situ wound dressing. *Mater. Today Bio* **2020**, *8*, 100074.

(22) Di Bella, C.; Duchi, S.; O'Connell, C. D.; Blanchard, R.; Augustine, C.; Yue, Z.; Thompson, F.; Richards, C.; Beirne, S.; Onofrillo, C.; Bauquier, S. H.; et al. In situ handheld three-dimensional bioprinting for cartilage regeneration. *J. Tissue Eng. Regen. Med.* **2018**, *12* (3), 611−621.

(23) Hakimi, N.; Cheng, R.; Leng, L.; Sotoudehfar, M.; Ba, P. Q.; Bakhtyar, N.; Amini-Nik, S.; Jeschke, M. G.; Günther, A. Handheld skin printer: in situ formation of planar biomaterials and tissues. *Lab Chip* **2018**, *18* (10), 1440−1451.

(24) Fortunato, G. M.; Rossi, G.; Bonatti, A. F.; De Acutis, A.; Mendoza-Buenrostro, C.; Vozzi, G.; De Maria, C. Robotic platform and path planning algorithm for in situ bioprinting. *Bioprinting* **2021**, *22*, No. e00139.

(25) A Levin, A.; A Karalkin, P.; V Koudan, E.; S Senatov, F.; A Parfenov, V.; A Lvov, V.; V Petrov, S.; D A S Pereira, F.; V Kovalev, A.; O Osidak, E.; P Domogatsky, S.; et al. Commercial articulated collaborative in situ 3D bioprinter for skin wound healing. *Int. J. Bioprint.* **2023**, *9* (2), 675.

(26) Fortunato, G. M.; Batoni, E.; Bonatti, A. F.; Vozzi, G.; De Maria, C. Surface reconstruction and tissue recognition for robotic-based in situ bioprinting. *Bioprinting* **2022**, *26*, No. e00195.

(27) Li, K.; Huang, W.; Guo, H.; Liu, Y.; Chen, S.; Liu, H.; Gu, Qi. Advancements in robotic arm-based 3D bioprinting for biomedical applications. *Life Med.* **2023**, *2* (6), lnad046.

(28) Thai, M. T.; Phan, P. T.; Tran, H. A.; Nguyen, C. C.; Hoang, T. T.; Davies, J.; Rnjak-Kovacina, J.; Phan, H. P.; Lovell, N. H.; Do, T. N. Advanced soft robotic system for in situ 3D bioprinting and endoscopic surgery. *Advanced Science* **2023**, *10* (12), 2205656.

(29) Verma, S.; Khanna, V.; Kumar, S.; Kumar, S. The Art of Building Living Tissues: Exploring the Frontiers of Biofabrication with 3D Bioprinting. *ACS Omega* **2023**, *8* (50), 47322−47339.

(30) Li, L.; Shi, J.; Ma, K.; Jin, J.; Wang, P.; Liang, H.; Cao, Y.; Wang, X.; Jiang, Q. Robotic in situ 3D bio-printing technology for repairing large segmental bone defects. *J. Adv. Res.* **2021**, *30*, 75−84.

(31) MacAdam, A.; Chaudry, E.; McTiernan, C. D.; Cortes, D.; Suuronen, E. J.; Alarcon, E. I. Development of in situ bioprinting: A mini review. *Front. Bioeng. Biotechnol.* **2022**, *10*, 940896.

(32) Matamoros, M.; Gómez-Blanco, J. C.; Sánchez, Á. J.; Mancha, E.; Marcos, A. C.; Carrasco-Amador, J. P.; Pagador, J. B. Temperature and humidity PID controller for a bioprinter atmospheric enclosure system. *Micromachines* **2020**, *11* (11), 999.

(33) Yang, S.; Chen, Q.; Wang, L.; Xu, M. In situ defect detection and feedback control with three-dimensional extrusion-based bioprinter-associated optical coherence tomography. *Int. J. Bioprint.* **2023**, *9* (1), 624.

(34) Fortunato, G. M.; Batoni, E.; Pasqua, I.; Nicoletta, M.; Vozzi, G.; De Maria, C. Automatic Photo-Cross-Linking System for Robotic-Based In Situ Bioprinting. *ACS Biomater. Sci. Eng.* **2023**, *9* (12), 6926−6934.

(35) Garciamendez-Mijares, C. E.; Guerra-Alvarez, G. E.; Sánchez-Salazar, M. G.; García-Rubio, A.; García-Martínez, G.; Mertgen, A. S.; Ceballos-González, C. F.; Bolivar-Monsalve, E. J.; Shrike Zhang, Y.; Santiago, G. T. d.; Alvarez, M. M. Development of an affordable extrusion 3D bioprinter equipped with a temperature-controlled printhead. *Int. J. Bioprint.* **2023**, *9* (6), 0244.

(36) Sanz-Garcia, A.; Sodupe-Ortega, E.; Pernía-Espinoza, A.; Shimizu, T.; Escobedo-Lucea, C. A versatile open-source printhead for low-cost 3D microextrusion-based bioprinting. *Polymers* **2020**, *12* (10), 2346.

(37) Ng, W. L.; Goh, G. L.; Goh, G. D.; Ten, J. S. J.; Yeong, W. Y. Progress and opportunities for machine learning in materials and processes of additive manufacturing. *Adv. Mater.* **2024**, *36*, 2310006.

(38) Jin, Z.; Zhang, Z.; Demir, K.; Gu, G. X. Machine learning for advanced additive manufacturing. *Matter* **2020**, *3* (5), 1541−1556.

(39) Zhang, J.; Li, H.; Ma, K.; Xue, L.; Han, B.; Dong, Y.; Tan, Y.; Gu, C. Design of PID temperature control system based on STM32. *IOP Conf. Ser. Mater. Sci. Eng.* **2018**, *322*, 072020.

(40) Xie, M.; Shi, Y.; Zhang, C.; Ge, M.; Zhang, J.; Chen, Z.; Fu, J.; Xie, Z.; He, Y. In situ 3D bioprinting with bioconcrete bioink. *Nat. Commun.* **2022**, *13* (1), 3597.

(41) Aldana, A. A.; Valente, F.; Dilley, R.; Doyle, B. Development of 3D bioprinted GelMA-alginate hydrogels with tunable mechanical properties. *Bioprinting* **2021**, *21*, No. e00105.

(42) Pepelanova, I.; Kruppa, K.; Scheper, T.; Lavrentieva, A. Gelatin-methacryloyl (GelMA) hydrogels with defined degree of functionalization as a versatile toolkit for 3D cell culture and extrusion bioprinting. *Bioengineering* **2018**, *5* (3), 55.

(43) Pereira, I.; Lopez-Martinez, M. J.; Villasante, A.; Introna, C.; Tornero, D.; Canals, J. M.; Samitier, J. Hyaluronic acid-based bioink improves the differentiation and network formation of neural progenitor cells. *Front. Bioeng. Biotechnol.* **2023**, *11*, 1110547.

(44) Stein, N.; Saathoff, T.; Antoni, S. T.; Schlaefer, A. Creating 3D gelatin phantoms for experimental evaluation in biomedicine. *Current Directions in Biomedical Engineering* **2015**, *1* (1), 331−334.

(45) Li, Q.; Zhang, B.; Xue, Q.; Zhao, C.; Luo, Y.; Zhou, H.; Ma, L.; Yang, H.; Bai, D. A systematic thermal analysis for accurately predicting the extrusion printability of alginate−gelatin-based hydrogel bioinks. *Int. J. Bioprint.* **2021**, *7* (3), 394.

(46) Walladbegi, J.; Schaefer, C.; Pernevik, E.; Sämfors, S.; Kjeller, G.; Gatenholm, P.; Sándor, G.; Rasmusson, L. Three-dimensional bioprinting using a coaxial needle with viscous inks in bone tissue engineering-an in vitro study. *Ann. Maxillofac Surg.* **2020**, *10* (2), 370−376.

(47) Liu, N.; Zhang, X.; Guo, Q.; Wu, T.; Wang, Y. 3D bioprinted scaffolds for tissue repair and regeneration. *Front. Mater.* **2022**, *9*, 925321.

(48) Ansari, M. A. A.; Golebiowska, A. A.; Dash, M.; Kumar, P.; Jain, P. K.; Nukavarapu, S. P.; Ramakrishna, S.; Nanda, H. S. Engineering biomaterials to 3D-print scaffolds for bone regeneration: practical and theoretical consideration. *Biomater. Sci.* **2022**, *10* (11), 2789−2816.

(49) Chung, J. J.; Im, H.; Kim, S. H.; Park, J. W.; Jung, Y. Toward biomimetic scaffolds for tissue engineering: 3D printing techniques in regenerative medicine. *Front. Bioeng. Biotechnol.* **2020**, *8*, 586406.

(50) Zhao, W.; Xu, T. Preliminary engineering for in situ in vivo bioprinting: a novel micro bioprinting platform for in situ in vivo bioprinting at a gastric wound site. *Biofabrication* **2020**, *12* (4), 045020.

(51) Wang, H.; Lian, Q.; Li, D.; Li, C.; Zhao, T.; Liang, J. Multi-tissue layering and path planning of in situ bioprinting for complex skin and soft tissue defects. *Rapid Prototyp. J.* **2021**, *27* (2), 321−332.

(52) Moon, S. H.; Hwang, H. J.; Jeon, H. R.; Park, S. J.; Bae, I. S.; Yang, Y. J. Photocrosslinkable natural polymers in tissue engineering. *Front. Bioeng. Biotechnol.* **2023**, *11*, 1127757.

(53) Choi, G.; Cha, H. J. Recent advances in the development of nature-derived photocrosslinkable biomaterials for 3D printing in tissue engineering. *Biomater. Res.* **2019**, *23* (1), 18.